

# Data-Driven Fine Element Tuning of Halide Double Perovskite for Enhanced Photoluminescence

Lingjun Wu, Zijian Chen, Zhongcheng Yuan, Bobin Wu, Shaohui Liu, Zixuan Wang, Jonathan P. Mailoa, Chenru Duan, Hao Huang,\* Chang-Yu Hsieh,\* Xue-Feng Yu,\* and Haitao Zhao\*

Element tuning of targeted materials and obtaining the optimal synthesis recipe are major goals for many material scientists. However, this is often limited by conventional trial-and-error procedures, which are time-consuming and labor-intensive. In this work, fine element tuning of halide double perovskite  $\text{Cs}_2\text{Na}_x\text{Ag}_{1-x}\text{In}_y\text{Bi}_{1-y}\text{Cl}_6$  is conducted by performing a data-driven investigation combining high-throughput experiments with machine learning (ML). A positive correlation between the more accessible R value in emission RGB values (the intensities of the red/green/blue primary colors) and photoluminescence intensity is revealed, and over a thousand R values of the  $\text{Cs}_2\text{Na}_x\text{Ag}_{1-x}\text{In}_y\text{Bi}_{1-y}\text{Cl}_6$  crystals synthesized with different additives and element compositions are collected. More importantly, the volume ratios of  $\text{Na}^+/\text{Ag}^+$  ( $V_{\text{Na}}:V_{\text{Ag}}$ ) and  $\text{Bi}^{3+}/\text{In}^{3+}$  ( $V_{\text{Bi}}:V_{\text{In}}$ ) with the corresponding R values are correlated through ML, and the synergistic regulation of the two ion pairs is revealed. A possible correlation between R and XRD is also proposed. Finally, different emission intensities of LED beads coated with  $\text{Cs}_2\text{Na}_x\text{Ag}_{1-x}\text{In}_y\text{Bi}_{1-y}\text{Cl}_6$  synthesized using parameters obtained from ML are demonstrated, and an emission enhancement of  $\approx 50$  times is observed between the brightest and dimmest LEDs. This work illustrates that data-driven investigation helps guide material synthesis and will significantly reduce the workload for developing novel materials, especially for complex compositions.

## 1. Introduction

In recent years, data-driven material research which benefits from interdisciplinary integration of material science and artificial intelligence (AI), greatly accelerates the pace of developing novel materials with desired properties.<sup>[1–8]</sup> Compared to the time-consuming and labor-intensive conventional trial-and-error procedures widely used in optimizing material synthesis, data-driven material research being able to process high-throughput data significantly decreases the workload. Especially, it becomes more powerful when multiple factors, e.g., the elements, compositions, etc., are taken into consideration.

Currently most data-driven material research are based on the combination of first-principle calculation and machine learning (ML).<sup>[9–11]</sup> Calculation is used to generate large amount of data, and ML is used to extract information from the big data. However, settings in calculations are often ideal and in actual experimental operations the situation may be more complicated. In this case, data-driven material research based on experimental

data sources is considered to be more reliable. However, obtaining large amount of reliable experimental data is challenging,

L. Wu, Z. Chen, B. Wu, S. Liu, Z. Wang, H. Huang, H. Zhao  
Materials Interfaces Center  
Shenzhen Institute of Advanced Technology  
Chinese Academy of Sciences  
Shenzhen, Guangdong 518055, P. R. China  
E-mail: hao.huang@siat.ac.cn; ht.zhao@siat.ac.cn

L. Wu, Z. Chen, B. Wu, S. Liu, Z. Wang, H. Zhao  
Center for Intelligent and Biomimetic Systems  
Shenzhen Institute of Advanced Technology  
Chinese Academy of Sciences  
Shenzhen, Guangdong 518055, P. R. China

Z. Chen  
Department of Chemical and Environmental Engineering  
The University of Nottingham Ningbo China  
Ningbo 315100, P. R. China

Z. Yuan  
Clarendon Laboratory  
Department of Physics  
University of Oxford  
Parks Road, Oxford OX1 3PU, UK

B. Wu, S. Liu  
Nano Science and Technology Institute  
University of Science and Technology of China  
Suzhou 215000, P. R. China

J. P. Mailoa  
Quantum Laboratory  
Tencent  
Shenzhen, Guangdong 518057, P. R. China

 The ORCID identification number(s) for the author(s) of this article can be found under <https://doi.org/10.1002/adom.202301245>

DOI: 10.1002/adom.202301245

and this limits the application of AI in experimental material research as well. Nonetheless, great efforts have been devoted into the experiment-based data-driven material research due to their great promise in material development.<sup>[3,12,13]</sup>

Among many materials, metal halide perovskite has attracted extensive attention from both academia and industry, and recent decades has witnessed a significant surge in their data-driven research.<sup>[14–17]</sup> Metal halide perovskites show great application potential in next-generation optoelectronic devices because of their tunable bandgaps, tolerance in defect, fast and balanced charge transport, and relatively low processing cost.<sup>[18–26]</sup> However, currently most data-driven research focuses on the lead-based halide perovskites, which suffer from high toxicity and instability, while the environmentally friendly halide double perovskites (HDP) are more promising because of their low toxicity and vast possible elemental compositions compared to their lead counterparts.

In this work, we conduct a case study of performing data-driven investigation on the element tuning of HDP  $\text{Cs}_2\text{Ag}_{1-x}\text{Na}_x\text{In}_{1-y}\text{Bi}_y\text{Cl}_6$  with a holistic strategy combining high-throughput chemical synthesis with optical characterizations. Thereafter, we perform ML modelling to establish the correlations between the precursor volume ratios and photoluminescence (PL) emission intensity. Further X-ray diffraction (XRD) results evidence the impact of precursor ratios on crystal structure and crystallinity, and the possible correlation between XRD and the PL intensity is also proposed. Finally, through the high-throughput element tuning, we obtain a series of  $\text{Cs}_2\text{Ag}_{1-x}\text{Na}_x\text{In}_{1-y}\text{Bi}_y\text{Cl}_6$  crystals with varied emission intensities, and we use them as phosphors in light-emitting diode (LED) beads for demonstrating their applications. We believe our data-driven material research here is instructive in HDP synthesis, and shall further inspire the research in other material systems.

## 2. Results and Discussion

### 2.1. The overall framework

In this work the data-driven element tuning of HDP is based on the high-throughput data collected using the in-situ synthesis

and characterization platform (Figure 1a). We show the crystal structure of the targeted material –  $\text{Cs}_2\text{Ag}_{1-x}\text{Na}_x\text{In}_{1-y}\text{Bi}_y\text{Cl}_6$  in Figure 1a, in which  $\text{Bi}^{3+}$  and  $\text{In}^{3+}$  are competitive ions and will replace each other's position in HDP structure (same case for  $\text{Na}^+$  and  $\text{Ag}^+$ ). Specifically, the high-throughput in-situ synthesis of  $\text{Cs}_2\text{Ag}_x\text{Na}_{1-x}\text{In}_y\text{Bi}_{1-y}\text{Cl}_6$  crystals with different additives or compositions are conducted in the multi-well plate.<sup>[3]</sup> After the synthesis process, the plates are further irradiated by a UV light source installed above, and the PL images are captured by a color-sensitive camera placed underneath. The camera records the R, G, B values (R, G, B values are the emission intensity of the three primary colors – red, green, and blue) of the photo automatically, making this home-built in situ RGB characterization platform highly convenient and able to collect massive data regarding emission intensities. Accordingly, we present the R values of each well in the plate in a heatmap to show the PL intensity distribution (Figure 1b).

The overall data-driven investigation process includes four main steps (Figure 1d), and in total over 1000 data points are collected. First, we conduct high-throughput screening of various additives (95 additives of various categories) to study their influence on the emission intensity of HDPs. Second, we perform a further investigation on the addition sequence of the  $\text{Na}^+$ -containing additives because of their excellent enhancement of HDP emissions. To reveal the role of different element ratios in the emission properties of HDPs, we perform both single-factor (tuning the relative adding volumes of  $\text{Bi}^{3+}$  and  $\text{In}^{3+}$  ( $V_{\text{Bi}}:V_{\text{In}}$ ) or  $\text{Na}^+$  and  $\text{Ag}^+$  ( $V_{\text{Na}}:V_{\text{Ag}}$ ) while keeping the other ion pair at constant) and double-factor (simultaneous tuning the relative volume ratios of two ion pairs ( $V_{\text{Bi}}:V_{\text{In}}$  and  $V_{\text{Na}}:V_{\text{Ag}}$ )) investigations. Next, we implement ML to build the correlation between R and the precursor ratios (i.e.,  $V_{\text{Bi}}:V_{\text{In}}$  and  $V_{\text{Na}}:V_{\text{Ag}}$ ). XRD is found to be highly intercorrelated with the precursor ratios, meanwhile the possible correlation between XRD and R is proposed (Figure 1c). Finally, we obtain the synthesis recipe (ideal  $V_{\text{Bi}}:V_{\text{In}}$  and  $V_{\text{Na}}:V_{\text{Ag}}$ ) for target HDP.

### 2.2. High-Throughput Screening of Additives and The Investigation on The Addition Sequence of The $\text{Na}^+$ -Containing Additives

It has been widely reported that additives play important roles in affecting perovskite crystal growing process and ensuing optoelectronics properties.<sup>[27,28]</sup> We start the data-driven investigation from high-throughput screening of various additives, including organic acids, esters, alcohols, sodium salts, potassium salts, amines, etc., which in total of 95 kinds, to screen out effective additives that enhance the HDP emission. We show all the structures of these 95 additives in Figure 2a. Four 24-well plates are used (denoted as plate 1, 2, 3, and 4). Within each well in the plates, we add same amount of the precursor solutions ( $\text{HCl}$ ,  $\text{CsCl}$ ,  $\text{AgCl}$ ,  $\text{InCl}_3$ ,  $\text{BiCl}_3$ ) as well as the specific additive, followed by the addition of the anti-solvent isopropanol to form the HDP crystals (details are included in Experimental Section in Supporting Information (SI)). The locations of the additives added are marked in Figure 2a, e.g., P1-A1 denotes that the additive is added into the A1 well in plate 1). The last well in plate 4 is used as reference without any additives (with same amount of  $\text{HCl}$  for

C. Duan  
Department of Chemical Engineering  
Massachusetts Institute of Technology  
Cambridge, MA 02139, USA  
C.-Y. Hsieh  
Innovation Institute for Artificial Intelligence in Medicine  
College of Pharmaceutical Sciences  
Zhejiang University  
Hangzhou 310058, P. R. China  
E-mail: kimhsieh@zju.edu.cn  
X.-F. Yu  
Shenzhen Key Laboratory of Micro/Nano Biosensing  
Shenzhen Institute of Advanced Technology  
Chinese Academy of Sciences  
Shenzhen, Guangdong 518055, P. R. China  
E-mail: xf.yu@siat.ac.cn  
X.-F. Yu  
Hubei Three Gorges Laboratory  
Yichang, Hubei 443007, P. R. China

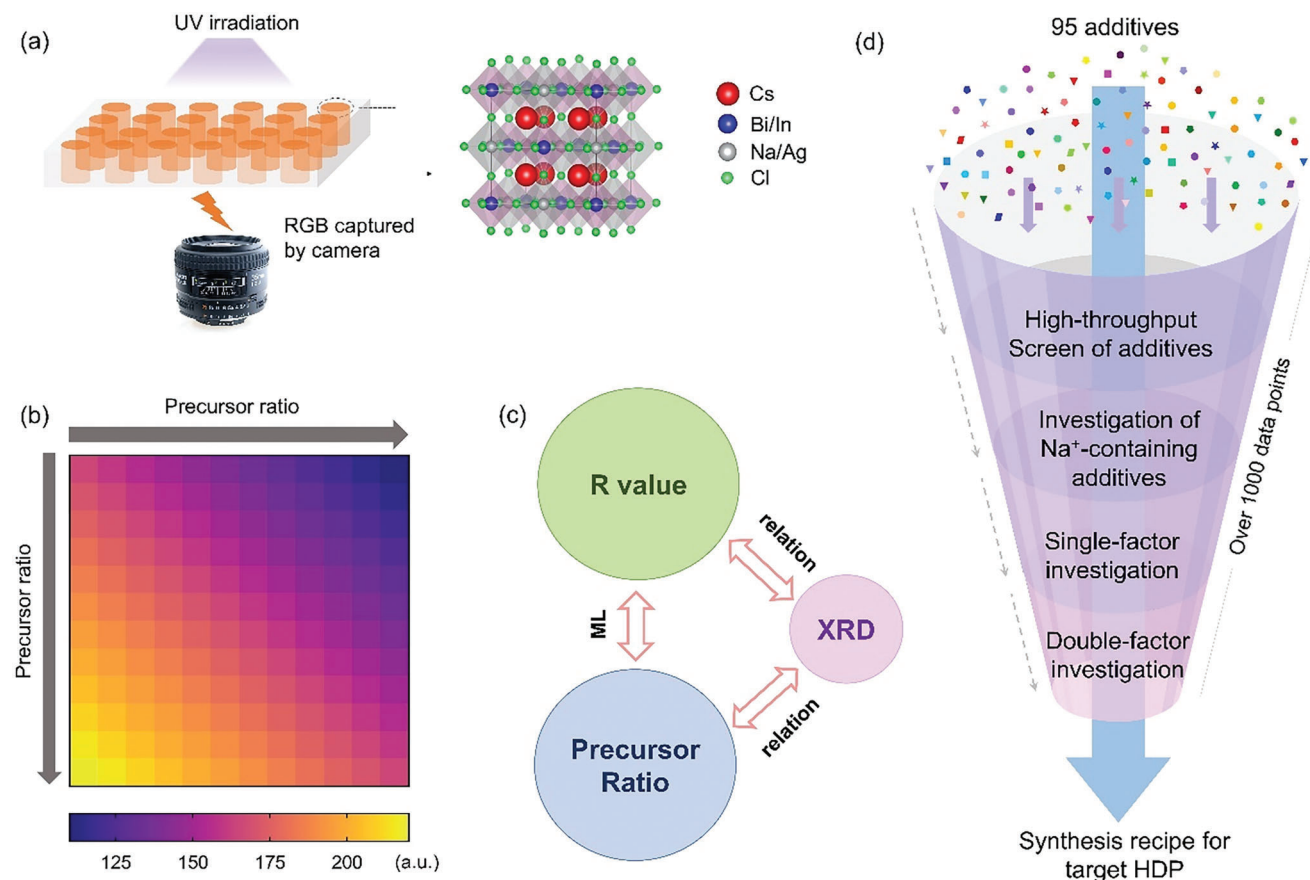


**Figure 1.** Data-driven high-throughput investigation of HDP. a) Scheme of the in-situ synthesis and RGB characterization platform. The crystal structure of HDP  $\text{Cs}_2\text{Ag}_x\text{Na}_{1-x}\text{In}_y\text{Bi}_{1-y}\text{Cl}_6$  is also shown; b) The schematic plot of the R value heatmap as collected by the camera, which demonstrate the overall trend in the plate; c) The R values are then used for ML modelling to establish the correlation with the precursor ratios. For XRD its relation with precursor ratios, as well as its possible correlation with R are proposed; d) The scheme of the entire data-driven investigation process in this work.

replacement). The details of the plate layout can be found in Table S1–S4 (Supporting Information).

We show the photos of the plates under UV irradiation in Figure 2b–e. As can be observed, samples with  $\text{Na}^+$ -containing additives in plate 3 (the well C3, C4, C5, C6, D1, D2, D3, and D4 highlighted in plate 3) show stronger emissions compared to the others. The corresponding additives are – sodium decyl sulfate, sodium oxalate, sodium methacrylate, sodium allylsulfonate, sodium 1-butanedisulfonate, sodium pentadisulfonate, sodium decane-1-sulfonate, and sodium lauroyl glutamate, which are denoted as Na1– Na8. This emission enhancement by  $\text{Na}^+$  could be attributed to the breakage of the inversion-symmetry-induced parity-forbidden transition and the reduced electronic dimensionality of HDP, which result in efficient radiative recombination of the self-trapped emission.<sup>[29,30]</sup>

After screening out the eight  $\text{Na}^+$ -containing additives, we are eager to know if the addition sequence of  $\text{Na}^+$  and the organic ligand have any significant effect on  $\text{Cs}_2\text{Ag}_x\text{Na}_{1-x}\text{In}_y\text{Bi}_{1-y}\text{Cl}_6$ , for there are a great number of possible species that can be formed through the combination of the elements in  $\text{Cs}_2\text{Ag}_x\text{Na}_{1-x}\text{In}_y\text{Bi}_{1-y}\text{Cl}_6$ , such as  $\text{Cs}_2\text{AgInCl}_6$ ,<sup>[31]</sup>  $\text{Cs}_2\text{AgBiCl}_6$ ,<sup>[32,33]</sup>  $\text{Cs}_2\text{NaInCl}_6$ ,<sup>[34]</sup>  $\text{Cs}_2\text{NaBiCl}_6$ , etc.<sup>[35,36]</sup> Therefore we further investigate the addition sequence of these  $\text{Na}^+$ -containing additives.

Using Na1 – Na8 as additives, the HDPs are prepared in two 24-well plates, named plate 5 and 6. Each row (A,B,C,D) in the plates represents one additive, and each column (1,2,3,4,5,6) represent one addition sequence of the corresponding additive (E.g., the sample in well A1 in plate 5 is synthesized using Na4 as additive, and the addition sequence is Na4-CsCl-AgCl-InCl<sub>3</sub>-BiCl<sub>3</sub>, and in A2, Na4 is added after CsCl, the addition sequence is CsCl-Na4-AgCl-InCl<sub>3</sub>-BiCl<sub>3</sub>, and so on, and for row B are samples with Na3 as the additive, see Tables S5,S6 (Supporting Information) for detailed plate layout and sequence). The last columns in two plates are the reference samples without additives for comparison.

While we are able to distinguish stronger emission from the photos in Figure 2, a more reliable method is necessary to characterize the emission intensity quantitatively. In this step, we extract the RGB values of each well in the plates from the images and compare them with the PL intensity. As shown in the PL spectra of samples in each well of plate 5 (Figure 3a), the PL emission peaks are located at  $\approx 40$  nm. And we further record the single-wavelength PL intensities at 640 nm (Figure 3b) to compare with the R,G,B values, respectively. We notice a positive correlation between PL intensity and RGB, as shown in Figure 3c, Figure S1a and S1b (Supporting Information).



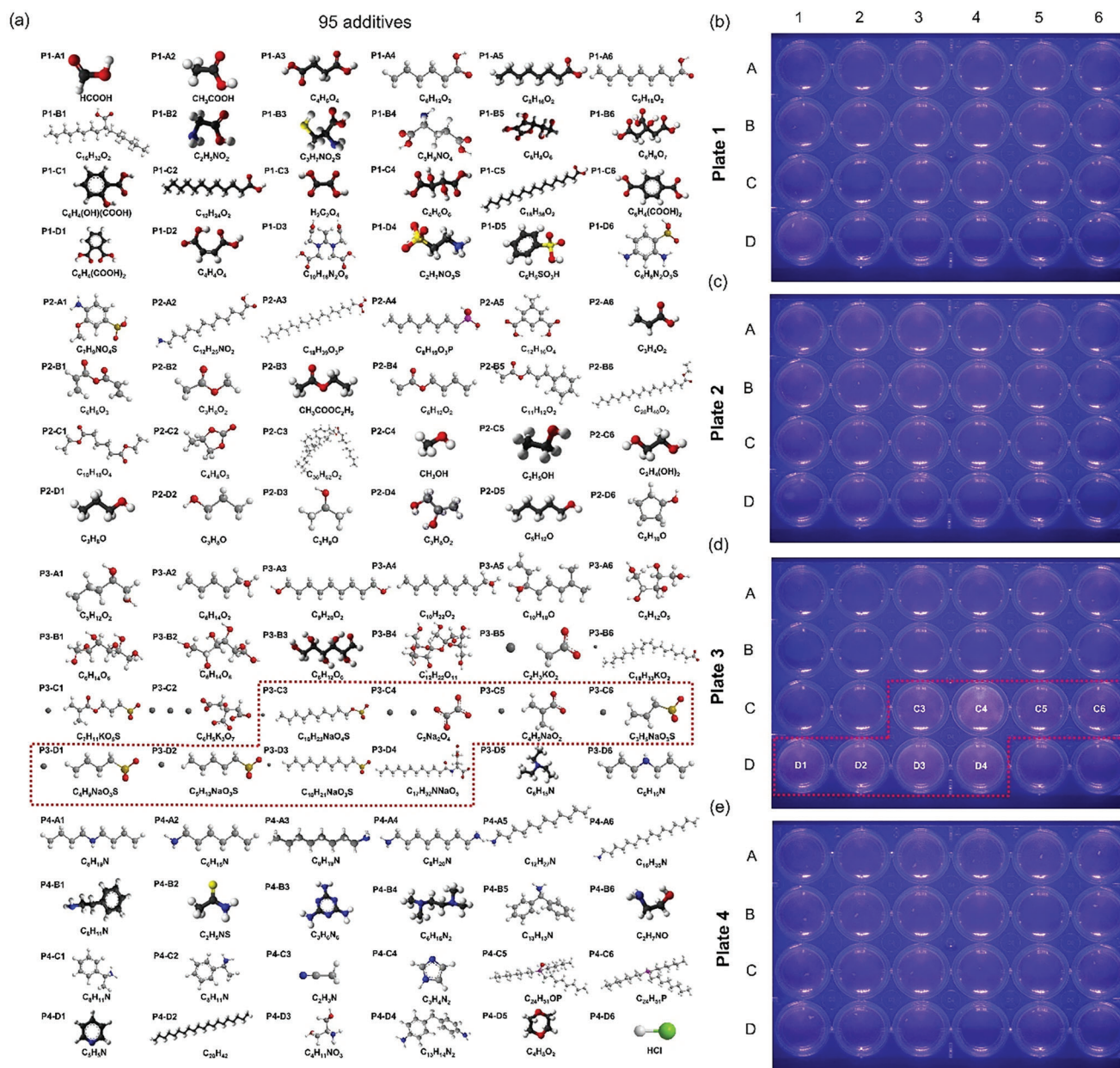


**Figure 2.** High-throughput screen of additives enhancing HDP emission. a) The structures of the additives investigated, the label Px-Ay represent their positions in the plate, e.g., P1-A1 refers to the A1 well in plate 1. The UV-photo of b) plate 1; c) plate 2; d) plate 3 and e) plate 4 under UV irradiation at 365 nm. A,B,C,D represents the 4 rows of the 24-well plate, and 1, 2, 3, 4, 5, 6 represent the columns.

Especially, the R values (Figure 3c) are more sensitive to the PL change as compared to the G (Figure S1a, Supporting Information) and B (Figure S1b, Supporting Information) values – the difference between the maximum and minimum R values  $\Delta R = 60$ , compared to  $\Delta G = 22$  and  $\Delta B = 18$  for G and B, respectively. We believe this is associated with PL emission peak locating  $\approx 640$  nm. Thus, we believe the R value is capable of reflecting the PL intensity of  $\text{Cs}_2\text{Ag}_{1-x}\text{Na}_x\text{In}_{1-y}\text{Bi}_y\text{Cl}_6$ . Compared to conventional PL measurement using spectrofluorometer, our in situ RGB value characterization is more convenient and allows in-situ characterization of multi-well plates.

We illustrate the UV-photo and the corresponding RGB values of plate 5 and 6 in Figure 3d and Figure S2 (Supporting Information) (details are summarized in Tables S9 and S10, Supporting Information). As can be observed from the figures, no apparent difference is observed between different columns, indicating the addition sequences of these  $\text{Na}^+$ -containing additives show weak effect on PL emission. While for the rows of these plates which represent different  $\text{Na}^+$ -containing additives, we observe the samples in row 3 of plate 5 with sodium oxalate (Na2) as the additive, outperforms the rest with the highest emission intensity (Figure 3d; Figure S2, Supporting Information). This improved

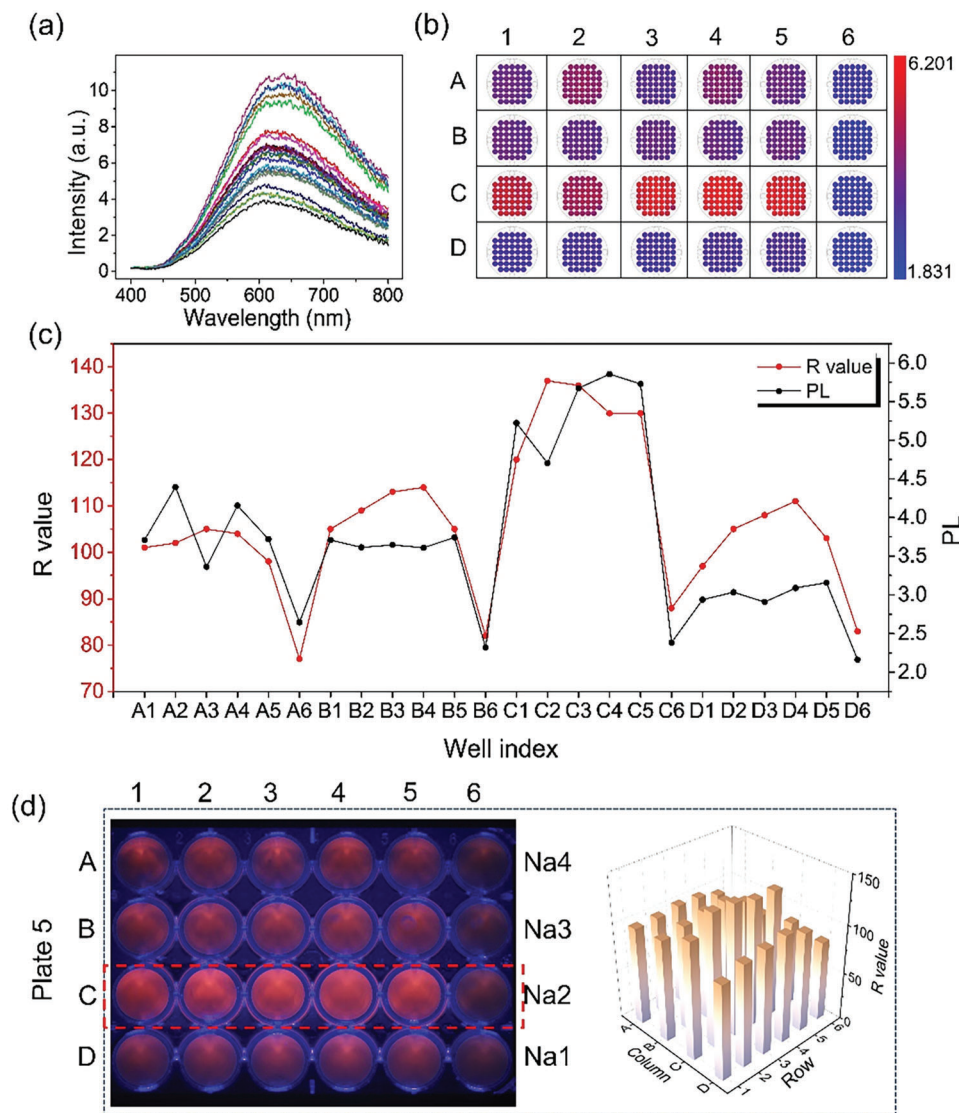


**Figure 3.** PL measurement versus RGB values of plate 5. a) PL spectra in the range of 400 – 800 nm; b) recording of PL intensities at single wavelength (640 nm); c) R value versus the single-wavelength (640 nm) PL; d) UV-photo of plate 5 investigating the Na<sup>+</sup>-containing additives Na<sub>4</sub>, Na<sub>3</sub>, Na<sub>2</sub>, Na<sub>1</sub>, and the corresponding R values.

emission intensity could be attributed to the existence of double Na<sup>+</sup> in sodium oxalate, which should facilitate the competitive occupying of Na<sup>+</sup> versus Ag<sup>+</sup>, and the proportion of Na<sup>+</sup> in the structure is assumed to increase, while the other mono-Na<sup>+</sup> additives show no significant differences among each other, indicating the organic ligands in these additives possibly play negligible role in affecting the PL emission of the HDPs. Hence sodium oxalate is used as the additive in the rest of this work.

### 2.3. Data-Driven High-Throughput Investigation of Precursor Volume Ratios

After we select sodium oxalate as the additive and prove the reliability of our high-throughput R recording platform, we further use it to perform fine element tuning in Cs<sub>2</sub>Ag<sub>1-x</sub>Na<sub>x</sub>In<sub>1-y</sub>Bi<sub>y</sub>Cl<sub>6</sub> to

obtain optimized recipe for the synthesis. Our results discussed above indicates that B(I) site in the HDP of type A<sub>2</sub>B(I)B(III)X<sub>6</sub> play a critical role in the emission properties, and the B(III) site also deserves in-depth exploration.<sup>[37]</sup> To get a systematic understanding of how these B site ions affect the HDP emission properties, we carry out high-throughput single/double-factor investigations on the added volume ratios of the two precursor ion pairs –V<sub>Na</sub>:V<sub>Ag</sub> and V<sub>Bi</sub>:V<sub>In</sub>.

First, we conduct single-factor tuning of V<sub>Na</sub>:V<sub>Ag</sub> to investigate the correlation between R with V<sub>Na</sub>:V<sub>Ag</sub>. Here 96 levels of V<sub>Na</sub>:V<sub>Ag</sub> ranging from 0:180 to 180:0 are prepared in a 96-well plate (plate 7) while V<sub>Bi</sub>:V<sub>In</sub> is kept at 90:90 for all wells. V<sub>Na</sub>:V<sub>Ag</sub> starts from 180:0 in H1, and V<sub>Na</sub>:V<sub>Ag</sub> decreases following a “zigzag” route, i.e., H1-G1-F1-D1-C1-B1-A1-A2-B2-C2-D2-E2-F2-G2-H2...H12, in this order until reaching the last well H12, V<sub>Na</sub>:V<sub>Ag</sub> decreases to 0:180. In each well, the total amount of V<sub>Na</sub>



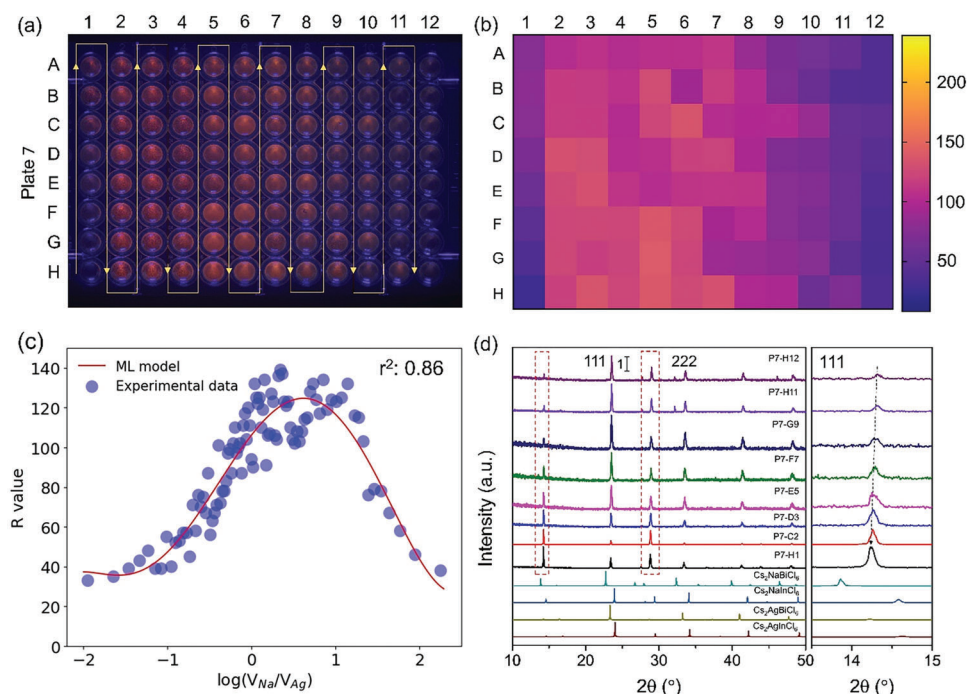


**Figure 4.** Single-factor investigation of  $V_{Na}:V_{Ag}$ . a) UV-photo of plate 7. A,B,C,D,E,F,G,H are the labels of the rows of plate 7, and 1, 2, 3, 4, 5, 6, 7, 8, 9, 10, 11, 12 are the labels of the columns. The “zig-zag” route of descending  $V_{Na}:V_{Ag}$  is shown in the photo; b) The corresponding heat map; c) ML modelling of the R value versus  $\log(V_{Na}/V_{Ag})$ ; d) Left: XRD patterns of selected samples from plate 7, right: the zoom-in view of peak 111.

and  $V_{Ag}$  is kept at 180  $\mu$ l (The detail values of  $V_{Na}:V_{Ag}$  for each well in plate 7 are given in Table S7, Supporting Information), while all the other reagents ( $CsCl$ ,  $BiCl_3$ ,  $InCl_3$ ,  $HCl$ ) are kept the same for all wells (See Supporting Information for more details of solutions). We show the UV photo of plate 7 in Figure 4a, from which a general trend of R can be observed, that higher R values are mostly centered in the region of medium high  $V_{Na}:V_{Ag}$ . This is more clearly illustrated in the heatmap of R values (Figure 4b), the color of samples turns bright reddish yellow as reflected by the increasing R with decreasing  $V_{Na}:V_{Ag}$  initially, then gradually turns blue violet with further decrease of  $V_{Na}:V_{Ag}$ . The RGB value of each well is given in Table S7 (Supporting Information).

We further conduct 10-fold cross-validation ML modelling to quantitatively correlate R with  $V_{Na}:V_{Ag}$ . In this work, the log values of precursor volume ratios are used in ML modelling for the consideration of data distribution. The data is divided into 9:1 as training set and testing set, respectively. The summary of ML is in Table S8 (Supporting Information). The cross-validation  $r^2$  is 0.86 for the training set and 0.83 for the testing set. The ML fitting versus experimental data are shown in Figure 4c. The HDP emission is weak ( $R < 60$ ) when  $V_{Na}:V_{Ag}$  is extremely low ( $V_{Na}:V_{Ag} = 0.01 - 0.1$ ), and R gradually increases with increasing  $V_{Na}:V_{Ag}$ , reaching the peak value at  $\approx 125$  with  $V_{Na}:V_{Ag} = 4.17$ . Over the peak value, R starts to decrease with further increasing  $V_{Na}:V_{Ag}$ . This may be ascribed to the reason that further increasing of  $Na^+$  content leads to higher non-radiative recombination rates.<sup>[38]</sup> The range of high R ( $R > 100$ ) is  $V_{Na}:V_{Ag} = 0.78 - 19.95$ . The correlation shows how HDP emission associate with changing  $V_{Na}:V_{Ag}$ .

To further obtain structural information, XRD patterns of several samples are collected, as shown in Figure 4d, peaks are all

normalized based on the (222) peak. Interestingly, we notice that the (111) peak intensities grow (from 0.533 to 1.542) and the peak positions shift to lower angles (14.32 to 14.23) along with increasing  $V_{Na}:V_{Ag}$  from 0: 180 to 180:0, as more clearly illustrated in the right subgraph in Figure 4d. The intensity and position of peak (111) are summarized in Table S9 (Supporting Information). The normalized peak intensity reflects the proportion of the two corresponding crystal faces of (111) and (222), indicating that increasing  $Na^+$  may lead to enhanced crystallinity of the (111) crystal face in HDPs. Moreover, the (111) peak intensity is also related to the B(I) and B(III) site ordering in  $A_2B(I)B(III)X_6$ .<sup>[29]</sup> Intensive (111) peak indicate well-ordered  $Bi^{3+}$  and  $Ag^+$  sites, while gets weaker with increasing  $In^{3+}$ ,<sup>[39]</sup> thus the peak growth with increasing  $V_{Na}:V_{Ag}$  observed here might be attributed to the increasing  $Ag^+$  which is isoelectronic to  $In^{3+}$ . The shifting of the (111) peak to lower  $2\theta$  with increasing  $V_{Na}:V_{Ag}$  is attributed to the lattice expansion due to the longer Na—Cl bond compared to the Ag—Cl bond.<sup>[40]</sup> The XRD result reveals how the HDP crystal structure is affected by  $V_{Na}:V_{Ag}$ .

Similar single-factor investigation on the tuning of  $V_{Bi}:V_{In}$  has been conducted in plate 8 (here  $V_{Na}:V_{Ag}$  is kept at 90:90), and different trend of R is observed. Low  $V_{Bi}:V_{In}$  is beneficial for enhancing the emission, while high  $V_{Bi}:V_{In}$  may in turn suppress the emission. The UV photo of plate 8 is shown in Figure S3a (Supporting Information).  $V_{Bi}:V_{In}$  also follows a “zigzag” route. In H1  $V_{Bi}:V_{In}$  is 180:0, and through the route H1-G1-F1-D1-C1-B1-A1-A2-B2-C2-D2-E2-F2-G2-H2...H12,  $V_{Bi}$  decreases while  $V_{In}$  increases with the total volume of  $V_{Bi}$  and  $V_{In}$  kept being 180  $\mu$ l, and till H12  $V_{Bi}:V_{In}$  is 0:180. Detailed values of  $V_{Bi}:V_{In}$  for each well in plate 8 and the RGB values are given in Table S10 (Supporting

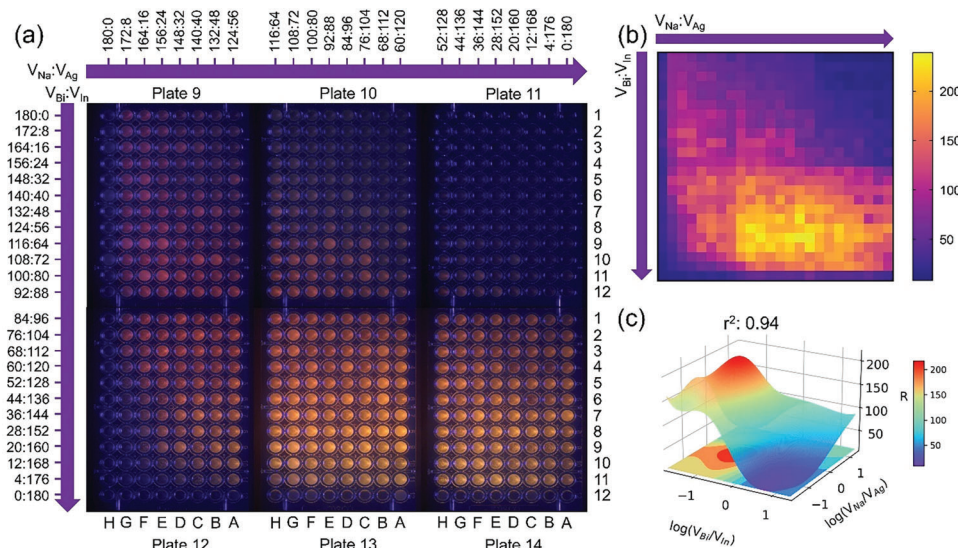


**Figure 5.** Double-factor investigation of  $V_{Na}:V_{Ag}$  and  $V_{Bi}:V_{In}$ . a) the UV-photo of the plate group for the double-factor investigation on  $V_{Na}:V_{Ag}$  and  $V_{Bi}:V_{In}$ . The arrows indicate the decreasing direction of  $V_{Na}:V_{Ag}$  or  $V_{Bi}:V_{In}$ , and the values of  $V_{Na}:V_{Ag}$  or  $V_{Bi}:V_{In}$  are also marked in the scales on the arrows; b) The corresponding heat map of the plate group; c) ML modelling of R versus  $\log(V_{Bi}/V_{In})$  and  $\log(V_{Na}/V_{Ag})$ .

Information). It can be observed that brighter emissions are centered in the region with lower  $V_{Bi}:V_{In}$ , which is further illustrated in the heatmap (Figure S3b, Supporting Information). Then 10-fold cross validation ML modelling the correlation between R and  $\log(V_{Bi}/V_{In})$  is conducted, as illustrated in Figure S3c (Supporting Information), a cross-validation  $r^2$  of 0.92 is reached for training and 0.86 for testing, the summary of the ML modelling is in Table S11 (Supporting Information). As shown in Figure S3c (Supporting Information), the maximum R is higher compared to that from the investigation on  $V_{Na}:V_{Ag}$  (Figure 4c). HDP with 0% Bi ( $Cs_2Na_xAg_{1-x}InCl_6$ ) content exhibits moderate emission with R of  $\approx 100$ , and with further increase in  $V_{Bi}:V_{In}$ , R increases and reaches the peak value at  $\approx 170$  when  $V_{Bi}:V_{In} = 0.178$ . R then decreases with further increase of  $V_{Bi}:V_{In}$ , and when  $V_{Bi}:V_{In} = 2.51$ , R drops to 100, reaching the same level to HDP with 0% Bi content, and further increase in  $V_{Bi}:V_{In}$  leads to the suppression of the emission. R finally decreases and stables at around 50 when  $V_{Bi}:V_{In} > 10$ . The range of high R ( $R > 135$ ) is  $V_{Bi}:V_{In} = 0.035 - 1.0$ . The addition of trace amount of  $Bi^{3+}$  helps improve the HDP crystallinity and leads to increased rate of radiative recombination, thus enhances the emission,<sup>[38]</sup> moreover the replacement of  $In^{3+}$  by  $Bi^{3+}$  breaks the parity-forbidden transition.<sup>[41]</sup> Meanwhile, the HDP emission is also proposed to be associated with its structural dynamics due to the stereoactivity of the lone pair of  $Bi^{3+}$ .<sup>[42]</sup> While the later declined emission might be attributed to the bandgap of HDP turning indirect with further increase of  $Bi^{3+}$ .<sup>[39,43]</sup>

Meanwhile, as shown in Figure S3d (Supporting Information), the growth of the (111) peak and its position shifting to lower  $2\theta$  values along the increase of  $V_{Bi}:V_{In}$  is also observed (information summarized in Table S12, Supporting Information), however the changes are greater compared to that observed with increasing  $V_{Na}:V_{Ag}$ . The (111) peak intensity grows from 0.289 to 1.859 when  $V_{Bi}:V_{In}$  increases from 0:180 to 180:0, shifting from 14.49 to 14.11. The growth in (111) intensity can be attributed

to the decrease in  $In^{3+}$ , and also indicates more formation of the (111) crystal surface. While the peak position shifts are attributed to the lattice expansion with increasing  $Bi^{3+}$  due to the larger size of  $Bi^{3+}$  compared to  $In^{3+}$ .<sup>[44]</sup> It can be noted that medium high  $Na^+$  content and lower  $Bi^{3+}$  content promote more intensive PL emission, agreeing well with previous study.<sup>[28,45,46]</sup>

The single factor investigation ( $V_{Na}:V_{Ag}$  or  $V_{Bi}:V_{In}$ ) results indicate that the ratios of these ions play critical roles in determining the emission properties of HDP. Considering that when tuning single ion pairs, the other ions might also influence the emission properties. Besides, to our best knowledge, single factor investigation of HDP have been relatively well studied in literature,<sup>[29,47]</sup> while a systematic and comprehensive study of the synergistic effect of both ion pairs is highly necessary yet remain unclear.

With the aid of our high-throughput in situ platform, we are able to perform the double-factor investigation on the element tuning of HDP, during which the HDP synthesis and characterization is performed in a wide window of ion ratios to investigate the synergistic effect of  $V_{Na}:V_{Ag}$  and  $V_{Bi}:V_{In}$ . Here we use six 96-well plates (plate 9 to 14) and combine them into a plate group. We set 24 levels for both  $V_{Na}:V_{Ag}$  (column) and  $V_{Bi}:V_{In}$  (row) ranging from 0:180 to 180:0 (details of each plate are given in Tables S13–S18, Supporting Information). We show the UV photo of the plate group in Figure 5a, from which we observe stronger PL intensities centered in the bottom middle part of the plate group (the detailed R values are summarized in Tables S19–S24, Supporting Information). We further plot the R values of the plate group in the heatmap (Figure 5b), which demonstrate the trend of R more clearly. The optimal  $V_{Na}:V_{Ag}$  shifts from high values for high  $V_{Bi}:V_{In}$  to medium values for low  $V_{Bi}:V_{In}$ , i.e., for the upper part of the heatmap with high  $V_{Bi}:V_{In}$ , the maximum PL occurs in the left side with higher  $V_{Na}:V_{Ag}$ ; whereas in the lower part of the heatmap when  $V_{Bi}:V_{In}$  values are low, the maximum PL occurs at more moderate  $V_{Na}:V_{Ag}$ .

The overall correlation between R and ion pair ratios is then constructed by conducting ML modelling, as shown in Figure 5c, the 3D surface shows the trend of R against  $\log(V_{\text{Na}}/V_{\text{Ag}})$  and  $\log(V_{\text{Bi}}/V_{\text{In}})$ . Cross-validation  $r^2$  of 0.94 and 0.93 are reached for the training and the testing set, respectively, suggesting good regression performance of the model (the cross-validation errors are summarized in Table S25, Supporting Information). As shown in Figure 5c, both regions of global maximum and minimum R are revealed by the ML model. The R maximum region ( $R > 200$ ) suggested by the model is centered in the region with  $V_{\text{Bi}}:V_{\text{In}} = 0.079 - 0.32$  and  $V_{\text{Na}}:V_{\text{Ag}} = 0.24 - 1.41$  (maximum  $R = 217.7$  with  $V_{\text{Bi}}:V_{\text{In}} = 0.17$  and  $V_{\text{Na}}:V_{\text{Ag}} = 0.65$ ), and the “valley” area ( $R < 20$ ) is in the region with  $V_{\text{Bi}}:V_{\text{In}} = 2.95 - 13.8$ , and  $V_{\text{Na}}:V_{\text{Ag}} = 0.02 - 0.15$  (minimum  $R = 9.7$  with  $V_{\text{Bi}}:V_{\text{In}} = 5.6$  and  $V_{\text{Na}}:V_{\text{Ag}} = 0.026$ ).

Besides, it can be observed from the overall trend of R that there appears to be subpeaks in the surface, i.e., the local maximums. We plot some of these subpeaks in Figure S4 (Supporting Information). These local maximums exhibit varying degrees of shifting when the controlled ion pair ratio changes, and  $V_{\text{Bi}}:V_{\text{In}}$  shows a greater impact on the shifting. As shown in Figure S4a (Supporting Information), the peak of R right-shifts with increasing  $V_{\text{Bi}}:V_{\text{In}}$ , indicating that when the Bi content in the system is high, basically higher Na is required to reach intensive emission. Moreover, high R peaks are observed in the range of low Bi content ( $V_{\text{Bi}}:V_{\text{In}}$  at 12:168 – 36:144). When  $V_{\text{Na}}:V_{\text{Ag}}$  is fixed, as shown in Figure S4b (Supporting Information), the R peak shift is not as apparent as that of changing  $V_{\text{Bi}}:V_{\text{In}}$ , only slight right-shift of the R peak is observed. Moreover, high R peaks are observed when  $V_{\text{Na}}:V_{\text{Ag}}$  is in the range of higher Na content ( $V_{\text{Na}}:V_{\text{Ag}}$  at 36:144 – 92:88). The double-factor tuning results strongly show the synergistic regulation effect of  $\text{Bi}^{3+}/\text{In}^{3+}$  and  $\text{Na}^+/\text{Ag}^+$  pairs, suggesting that synthesizing multi-elements HDPs through conventional control variables might not be able to fully reveal the optimal compositions.

Some of the SEM of samples from the plate group is shown in Figure S5 (Supporting Information), as can be observed high crystal quality of the HDP microcrystals has been achieved with diverse size ranging from 1 to 5  $\mu\text{m}$ . Following previous discussion, we collect XRD patterns of selected samples from the plate group. These samples are distributed evenly in the plate group as shown in Figure S6 (Supporting Information). The XRD patterns for samples positioned on the two diagonal lines of the plate group are shown in Figure S7 (Supporting Information). The relevant data are summarized in Tables S26 and S27 (Supporting Information).

Figure S7 (Supporting Information) demonstrate the larger impact of  $V_{\text{Bi}}:V_{\text{In}}$  on the HDP structure compared to  $V_{\text{Na}}:V_{\text{Ag}}$ . Figure S7a (Supporting Information) shows the XRD patterns of samples with both increasing  $V_{\text{Bi}}:V_{\text{In}}$  and  $V_{\text{Na}}:V_{\text{Ag}}$ . As discovered in the single-factor investigations, the (111) peak grows and shifts to lower  $2\theta$  with increasing  $V_{\text{Bi}}:V_{\text{In}}$  or  $V_{\text{Na}}:V_{\text{Ag}}$ . Therefore, for the concurrent increase of  $V_{\text{Bi}}:V_{\text{In}}$  and  $V_{\text{Na}}:V_{\text{Ag}}$ , significant growth of (111) peak ( $\Delta = 1.605$ ) and position shift ( $\Delta = -0.49$ ) have been observed (relevant data summarized in Table S30, Supporting Information). We further observe the (111) peak grows ( $\Delta = 0.387$ ) and shifts to lower  $2\theta$  ( $\Delta = -0.33$ ) (relevant data summarized in Table S27, Supporting Information) in a less obvious trend, when  $V_{\text{Bi}}:V_{\text{In}}$  increases and  $V_{\text{Na}}:V_{\text{Ag}}$  decreases (Figure S7b, Sup-

porting Information). Meanwhile, XRD of double-factor samples with one ion pair fixed show the same trend discovered in the single-factor investigations, as shown in Figures S8–S12 (Supporting Information).

The synergistic effect of  $V_{\text{Bi}}:V_{\text{In}}$  and  $V_{\text{Na}}:V_{\text{Ag}}$  on XRD is more clearly demonstrated in the 2D scatter plot of all XRD data distributed over the full range of  $V_{\text{Bi}}:V_{\text{In}}$  and  $V_{\text{Na}}:V_{\text{Ag}}$ , as shown in Figures S13 and S14 (Supporting Information). Meanwhile, we plot the 2D scatter plot of R versus XRD intensity ( $I_{\text{XRD}}$ ) and position ( $P_{\text{XRD}}$ ) in Figure S15 (Supporting Information), as can be observed high R values mainly centered in the region with medium to high  $P_{\text{XRD}}$  at  $\approx 14.35 - 14.45$ , and  $I_{\text{XRD}} \approx 0.2 - 0.6$ . Some points in this region may correspond to HDPs with low  $V_{\text{Bi}}:V_{\text{In}}$  and medium  $V_{\text{Na}}:V_{\text{Ag}}$ , and we know that this is beneficial for enhanced HDP emission. Points in region with lower  $I_{\text{XRD}}$  and  $P_{\text{XRD}}$  are the HDPs with extremely low  $V_{\text{Bi}}:V_{\text{In}}$  and  $V_{\text{Na}}:V_{\text{Ag}}$ , while points in the region with higher  $I_{\text{XRD}}$  and  $P_{\text{XRD}}$  are the HDPs with high/medium  $V_{\text{Bi}}:V_{\text{In}}$  and  $V_{\text{Na}}:V_{\text{Ag}}$ . Figure S15 (Supporting Information) demonstrate the potential direct association between HDP emission with its structure. However, it needs to be point out that more data is required to further verify this association. Here we propose the possible trend using our limited but evenly distributed data.

We further utilize HDP with various emission intensities as fluorescent layers on top of commercial blue LED beads, and demonstrate their application potential for lighting. The HDP are synthesized based on the synthesis recipe ( $V_{\text{Bi}}:V_{\text{In}}$  and  $V_{\text{Na}}:V_{\text{Ag}}$ ) obtained from the R – ion ratio correlation from our double-factor investigation, and the process is illustrated in Figure S16a (Supporting Information). Their detailed synthesis procedures and parameters are summarized in the Experimental Section and Table S33 (Supporting Information). It needs to be point out that both  $V_{\text{Na}}:V_{\text{Ag}}$  and  $V_{\text{Bi}}:V_{\text{In}}$  of sample 5 fall into the global maximum R region in Figure 5c. As shown in the inset in Figure S16b (Supporting Information), the LED beads with these five HDP samples as the fluorescent layers are denoted as light 1,2,3,4,5, respectively, together with a bear LED bead as reference. We show the emission spectra of the five LED beads in Figure S16b (Supporting Information). Especially, light 5 shows much more intensive emission, which is  $\approx 50$  times more emissive than that of light 1 at  $\lambda = 640 \text{ nm}$ .

### 3. Conclusion

In this work, a data-driven investigation of the element tuning of HDP ( $\text{Cs}_2\text{Ag}_{1-x}\text{Na}_x\text{In}_{1-y}\text{Bi}_y\text{Cl}_6$ ) is presented. First, high-throughput screening of 95 additives is carried out, and the  $\text{Na}^+$ -containing additives stand out for their excellent enhancement of PL. Further investigation of the addition sequence of these  $\text{Na}^+$ -containing additives and the remarkable performance of sodium oxalate indicate the significance of the B(I) and B(III) sites for the  $\text{A}_2\text{B}(\text{I})\text{B}(\text{III})\text{X}_6$  type HDP's optical property. High-throughput single/double-factor investigations on the precursor volume ratios are performed for the fine element tuning of HDP. The correlations between the R values and precursor volume ratios are established via ML. Local maximum R of single-factor investigations are obtained, while ML modelling of double-factor investigations reveals the global maximum values as well as the overall trend.  $V_{\text{Bi}}:V_{\text{In}}$  is found to exert more significant impact



on the structure of HDP compared to  $V_{Na}:V_{Ag}$  as revealed by XRD. The association between R and XRD is proposed. Finally, the LED application of HDPs synthesized based on ML results is demonstrated. We believe the data-driven investigation in our work shows great guiding significance in HDP studies, and has the potential to be extended to the development of other material system.

## Supporting Information

Supporting Information is available from the Wiley Online Library or from the author.

## Acknowledgements

L.W., Z.C., and Z.Y. contributed equally to this work. This work was supported by the National Natural Science Foundation of China (52173234), the Shenzhen Science and Technology Program (grant no. RCJC20200714114435061), the Shenzhen Science and Technology Program (JCY20210324102008023 and JSGG20210802153408024), the Shenzhen-Hong Kong-Macau Technology Research Program (Type C, SGDX2020110309300301), the Natural Science Foundation of Guangdong Province (2022A1515010554 and 2022A1515011959), the Open Project of Zhengzhou JiShu Institute of AI Science (ZZJSB2023001), the European Union's Horizon 2020 research and innovation program under grant agreement no. 861985 (PEROCUBE), the innovation programme under Marie Skłodowska-Curie grant agreement no. 101105627, the Engineering and Physical Sciences Research Council (UK) (grant EP/Y029135/1), and the CCF-Tencent Open Fund.

## Conflict of Interest

The authors declare no conflict of interest.

## Data Availability Statement

The data that support the findings of this study are available in the supplementary material of this article.

## Keywords

data-driven, double halide perovskites, high-throughput, photoluminescence, synthesis design

Received: August 22, 2023  
Published online: October 5, 2023

- [1] Z. Wang, Z. Sun, H. Yin, X. Liu, J. Wang, H. Zhao, C. H. Pang, T. Wu, S. Li, Z. Yin, X.-F. Yu, *Adv. Mater.* **2022**, *34*, 2104113.
- [2] Y. Yao, Q. i Dong, A. Brozena, J. Luo, J. Miao, M. Chi, C. Wang, I. G. Kevrekidis, Z. J. Ren, J. Greeley, G. Wang, A. Anapolsky, L. Hu, *Science* **2022**, *376*, eabn3103.
- [3] H. Zhao, W. Chen, H. Huang, Z. Sun, Z. Chen, L. Wu, B. Zhang, F. Lai, Z. Wang, M. L. Adam, C. H. Pang, P. K. Chu, Y. Lu, T. Wu, J. Jiang, Z. Yin, X.-F. Yu, *Nat. Synth.* **2023**, *2*, 505.
- [4] A. L. Ferguson, K. A. Brown, *Annu. Rev. Chem. Biomol. Eng.* **2022**, *13*, 25.

- [5] M. Abolhasani, K. A. Brown, *MRS Bull.* **2023**, *48*, 134.
- [6] Q. Liang, A. E. Gongora, Z. Ren, A. Tiihonen, Z. Liu, S. Sun, J. R. Deneault, D. Bash, F. Mekki-Berrada, S. A. Khan, K. Hippalgaonkar, B. Maruyama, K. A. Brown, J. Fisher III, T. Buonassisi, *npj Comput. Mater.* **2021**, *7*, 188.
- [7] B. Maruyama, J. Hattrick-Simpers, W. Musinski, L. Graham-Brady, K. Li, J. Hollenbach, A. Singh, M. L. Taheri, *MRS Bull.* **2022**, *47*, 1154.
- [8] L. Wu, Z. Xu, Z. Wang, Z. Chen, Z. Huang, C. Peng, X. Pei, X. Li, J. P. Mailoa, C.-Y. Hsieh, T. Wu, X.-F. Yu, H. Zhao, *Sci. China Technol. Sci.* **2022**, *65*, 2274.
- [9] X. Cai, Y. Zhang, Z. Shi, Y. Chen, Y. Xia, A. Yu, Y. Xu, F. Xie, H. Shao, H. Zhu, D. Fu, Y. Zhan, H. Zhang, *Adv. Sci.* **2022**, *9*, 2103648.
- [10] J. Kim, K. Min, *Adv. Theory Simul.* **2022**, *5*, 2200068.
- [11] H. Zhao, C. I. Ezech, W. Ren, W. Li, C. H. Pang, C. Zheng, X. Gao, T. Wu, *Appl. Energy* **2019**, *254*, 113651.
- [12] F. Lai, Z. Sun, S. E. Saji, Y. He, X. Yu, H. Zhao, H. Guo, Z. Yin, *Small* **2021**, *17*, 2100024.
- [13] X. Du, L. Luer, T. Heumueller, J. Wagner, C. Berger, T. Osterrieder, J. Wortmann, S. Langner, U. Vongsaysy, M. Bertrand, N. Li, T. Stubhan, J. Hauch, C. J. Brabec, *Joule* **2021**, *5*, 495.
- [14] K. Higgins, M. Ziatdinov, S. V. Kalinin, M. Ahmadi, *J. Am. Chem. Soc.* **2021**, *143*, 19945.
- [15] Y. Zhao, J. Zhang, Z. Xu, S. Sun, S. Langner, N. T. P. Hartono, T. Heumueller, Y. i Hou, J. Elia, N. Li, G. J. Matt, X. Du, W. Meng, A. Osvet, K. Zhang, T. Stubhan, Y. Feng, J. Hauch, E. H. Sargent, T. Buonassisi, C. J. Brabec, *Nat. Commun.* **2021**, *12*, 2191.
- [16] L. Zhang, N. a Li, D. Liu, G. Tao, W. Xu, M. Li, Y. Chu, C. Cao, F. Lu, C. Hao, J. u Zhang, Y. Cao, F. Gao, N. Wang, L. Zhu, W. Huang, J. Wang, *Angew. Chem., Int. Ed.* **2022**, *61*, e202209337.
- [17] Y. Li, Y. Lu, X. Huo, D. Wei, J. Meng, J. Dong, B. Qiao, S. Zhao, Z. Xu, D. Song, *RSC Adv.* **2021**, *11*, 15688.
- [18] J. J. Yoo, G. Seo, M. R. Chua, T. G. Park, Y. Lu, F. Rotermund, Y.-K. Kim, C. S. u Moon, N. J. Jeon, J.-P. Correa-Baena, V. Bulovic, S. S. Shin, M. G. Bawendi, J. Seo, *Nature* **2021**, *590*, 587.
- [19] H. Ling, J. Wu, F. Su, Y. Tian, Y. J. Liu, *Nat. Commun.* **2021**, *12*, 1010.
- [20] Y. Zhao, T. Heumueller, J. Zhang, J. Luo, O. Kasian, S. Langner, C. Kupfer, B. Liu, Y. Zhong, J. Elia, A. Osvet, J. Wu, C. Liu, Z. Wan, C. Jia, N. Li, J. Hauch, C. J. Brabec, *Nat. Energy* **2022**, *7*, 144.
- [21] J. Li, L. Xu, T. Wang, J. Song, J. Chen, J. Xue, Y. Dong, B. o Cai, Q. Shan, B. Han, H. Zeng, *Adv. Mater.* **2017**, *29*, 1603885.
- [22] S. D. Stranks, H. J. Snaith, *Nat. Nanotechnol.* **2015**, *10*, 391.
- [23] J. Zhao, L. Zhao, Y. Deng, X. Xiao, Z. Ni, S. Xu, J. Huang, *Nat. Photonics* **2020**, *14*, 612.
- [24] Y. Zhou, J. Chen, O. M. Bakr, O. F. Mohammed, *ACS Energy Lett.* **2021**, *6*, 739.
- [25] H. Zhu, Y. Fu, F. Meng, X. Wu, Z. Gong, Q. i Ding, M. V. Gustafsson, M. T. Trinh, S. Jin, X.-Y. Zhu, *Nat. Mater.* **2015**, *14*, 636.
- [26] N. Zhang, Y. Fan, K. Wang, Z. Gu, Y. Wang, L. i Ge, S. Xiao, Q. Song, *Nat. Commun.* **2019**, *10*, 1770.
- [27] Q. Hu, G. Niu, Z. Zheng, S. Li, Y. Zhang, H. Song, T. Zhai, J. Tang, *Small* **2019**, *15*, 1903496.
- [28] Y. Liu, Y. Jing, J. Zhao, Q. Liu, Z. Xia, *Chem. Mater.* **2019**, *31*, 3333.
- [29] J. Luo, X. Wang, S. Li, J. Liu, Y. Guo, G. Niu, L. i Yao, Y. Fu, L. Gao, Q. Dong, C. Zhao, M. Leng, F. Ma, W. Liang, L. Wang, S. Jin, J. Han, L. Zhang, J. Etheridge, J. Wang, Y. Yan, E. H. Sargent, J. Tang, *Nature* **2018**, *563*, 541.
- [30] S. Li, J. Luo, J. Liu, J. Tang, *J. Phys. Chem. Lett.* **2019**, *10*, 1999.
- [31] J. C. Dahl, W. T. Osowiecki, Y. Cai, J. K. Swabeck, Y. Bekenstein, M. Asta, E. M. Chan, A. P. Alivisatos, *Chem. Mater.* **2019**, *31*, 3134.
- [32] B. Yang, J. Chen, S. Yang, F. Hong, L. Sun, P. Han, T. Pullerits, W. Deng, K. Han, *Angew. Chem., Int. Ed.* **2018**, *57*, 5359.
- [33] S. E. Creutz, E. N. Crites, M. C. De Siena, D. R. Gamelin, *Nano Lett.* **2018**, *18*, 1118.

- [34] P. Han, X. Mao, S. Yang, F. Zhang, B. Yang, D. Wei, W. Deng, K. Han, *Angew. Chem.* **2019**, *131*, 17391.
- [35] R. S. Lamba, P. Basera, S. Bhattacharya, S. Sapra, *J. Phys. Chem. Lett.* **2019**, *10*, 5173.
- [36] P. Han, X. Zhang, C. Luo, W. Zhou, S. Yang, J. Zhao, W. Deng, K. Han, *ACS Cent. Sci.* **2020**, *6*, 566.
- [37] B. Yang, X. Mao, F. Hong, W. Meng, Y. Tang, X. Xia, S. Yang, W. Deng, K. Han, *J. Am. Chem. Soc.* **2018**, *140*, 17001.
- [38] Y. Liu, A. Nag, L. Manna, Z. Xia, *Angew. Chem., Int. Ed.* **2021**, *60*, 11592.
- [39] A. Karmakar, G. M. Bernard, A. Meldrum, A. O. Oliynyk, V. K. Michaelis, *J. Am. Chem. Soc.* **2020**, *142*, 10780.
- [40] S. Xue, Q. Wu, Q. Huo, J. Mi, C. Guan, W.-Y. Cong, Z. Zhang, J. Ren, Y.-B. Lu, *Phys. Chem. Chem. Phys.* **2022**, *24*, 25648.
- [41] P. Han, X. Zhang, X. Mao, B. Yang, S. Yang, Z. Feng, D. Wei, W. Deng, T. Pullerits, K. Han, *Sci. China Chem.* **2019**, *62*, 1405.
- [42] K. M. McCall, V. Morad, B. M. Benin, M. V. Kovalenko, *ACS Mater. Lett.* **2020**, *2*, 1218.
- [43] E. T. McClure, M. R. Ball, W. Windl, P. M. Woodward, *Chem. Mater.* **2016**, *28*, 1348.
- [44] J. Xu, G. Chen, T. Yang, H. Wu, L. Li, C. Ma, C. Zhu, Y. Wu, B. Liu, A. Hu, X. Qiu, L. Zhong, J. Shen, A. Huang, Y. Guo, H. Gao, *J. Lumin.* **2023**, *255*, 119606.
- [45] O. Stroyuk, O. Raievska, P. Sebastia-Luna, B. A. H. Huisman, C. Kupfer, A. Barabash, J. Hauch, H. J. Bolink, C. J. Brabec, *ACS Mater. Lett.* **2023**, *5*, 596.
- [46] O. Stroyuk, O. Raievska, A. Barabash, M. Batentschuk, A. Osvet, S. Fiedler, U. Resch-Genger, J. Hauch, C. J. Brabec, *J. Mater. Chem. C* **2022**, *10*, 9938.
- [47] M.-M. Yao, L. Wang, J.-S. Yao, K.-H. Wang, C. Chen, B.-S. Zhu, J.-N. Yang, J.-J. Wang, W.-P. Xu, Q. Zhang, H.-B. Yao, *Adv. Opt. Mater.* **2020**, *8*, 1901919.